Journal of Applied Mechanics and Technical Physics, Vol. 39, No. 2, 1998

EXPERIMENTAL STUDY AND MATHEMATICAL SIMULATION OF THE CHARACTERISTICS OF A TURBULENT FLOW IN A STRAIGHT CIRCULAR PIPE ROTATING ABOUT ITS LONGITUDINAL AXIS

P. G. Zaets, A. F. Kurbatskii,[1] A. T. Onufriev, S. V. Poroseva,[2]
N. A. Safarov, R. A. Safarov, and S. N. Yakovenko[1]

UDC 532.517.4

The vorticity formed in the cross section of a turbulent flow in a straight circular pipe rotating about its longitudinal axis decreases the values of the turbulent stresses, turbulence energy, and dissipation rate along the pipe. The results of laboratory experiments and calculations by the second-order closure model of turbulent transfer are presented. On the whole, the model using a system of transport equations yields better agreement with experimental data than the models with algebraic relations for second-order moments.

Introduction. The action of mass forces in a swirling flow (centrifugal and Coriolis accelerations), which is similar to the action of the acceleration of gravity in a stratified flow [1, 2], weakens momentum and heat-transfer processes. The vorticity formed in the cross section of a turbulent flow in a straight circular pipe rotating about its longitudinal axis suppresses turbulent fluctuations and radial turbulent transfer at small and moderate velocities of pipe rotation: the turbulent stress, the turbulence energy, and its dissipation decrease.

Onufriev and Khristianovich [3, 4] considered the influence of the swirling flow on its statistical characteristics on the basis of semi-empirical equations that describe the behavior of the mean velocity fields and the second-order moments in the local-equilibrium approximation.

We present the data of laboratory measurements of the first- and second-order moments of the velocity field for a flow of an incompressible liquid in a motionless and rotating pipe. These data are compared with the calculation results obtained using three models of turbulent transfer. These models include differential transport equations for the components of the Reynolds stress tensor, algebraic relationships for normal turbulent stresses in the nonequilibrium approximation, and algebraic relationships for turbulent stresses in the local-equilibrium approximation, respectively.

The experimental hot-wire anemometry results were obtained at the Moscow Physicotechnical Institute, and the calculations were performed at the Institute of Theoretical and Applied Mechanics of the Siberian Division of the Russian Academy of Sciences and Novosibirsk State University.

Experimental Study of the Turbulent Flow Characteristics in a Rotating Pipe. The experiments were performed on a setup whose main units were the straight section of a channel whose length was equal to 100 diameters and which formed a developed turbulent flow and the rotating section, which was 25 diameters long (the channel diameter was 0.06 m). The air was injected into the channel from a high-pressure pipeline through a reductor and a flow governor, which ensured a constant flow rate. The temperature of the air injected into the channel was maintained constant and equal to room temperature by means of an automatically adjusted heater. After the heater, the air entered a receiver wherein it passed

Moscow Physicotechnical Institute, Dolgoprudnyi 141700. [1]Institute of Theoretical and Applied Mechanics, Siberian Division, Russian Academy of Sciences, Novosibirsk 630090. [2]Novosibirsk State University, Novosibirsk 630090. Translated from Prikladnaya Mekhanika i Tekhnicheskaya Fizika, Vol. 39, No. 2, pp. 103–116, March–April, 1998. Original article submitted July 11, 1996.

0021-8944/98/3902-0249 $20.00

through several layers of nylon cloth and the equalizing metal grids. The receiver was connected to the flow-forming section by a nozzle with contraction 12 : 1. A turbulizer was placed between the nozzle and the channel entrance. The regime of developed turbulent flow for a given Reynolds number was achieved at the end of the motionless section of the pipe. The flow with these characteristics entered the test section of the channel, which could rotate about the centerline. The rotated section was driven by an asynchronous engine with frequency control of the rotation velocity within the range 0 to 70 revolutions per second. The flow velocity U_0 at the channel axis varied from 0 to 70 m/sec. The swirling level can be characterized by the parameter $SP = W_0/U_0 = \omega R/U_0$, where ω is the angular velocity of pipe rotation. The measurement results presented below were obtained for $U_0 = 10$ m/sec and $Re_D = U_0 2R/\nu = 4 \cdot 10^4$ (ν is the kinematic viscosity of the air and R is the pipe radius).

The turbulent flow characteristics were measured by DISA hot-wire equipment; 55P11 single-wire, 55P61 double-wire, and 55P91 triple-wire probes were used. The signals were registered by analog devices and processed on a dedicated "PLURIMAT-S" mini-computer with temporal recording of the signals. The setup and the measurement technique are described in more detail in [5–8]. The longitudinal and circumferential components of the mean velocity, the components of the Reynolds stress tensor, some third-order moments, and the energy dissipation rate were measured based on the dependence for the longitudinal one-dimensional spectrum.

Model of the Transport Equations for Turbulent Stress. We use three turbulent transfer models of different complexity to describe the behavior of the first- and second-order moments of the velocity field of a turbulent flow in a round pipe rotating about its axis. The goal is to clarify the accuracy of these models.

Model No. 1 includes the differential equations of turbulent transfer for the mean velocity vector and turbulent stress tensor [9–11]. Simplified variants of this complete model are obtained if the differential equations for the sought second-order moments are somehow reduced to algebraic relationships. Model No. 2 of turbulent transfer was developed [9, 12] by simplifying the equations for the Reynolds stress-tensor components in the local-equilibrium approximation for tangential stresses and in the nonequilibrium approximation for normal stresses. Model No. 3 contains the relationships determined from the transport equations for the second-order moments in the local-balance approximation for all the components of the turbulent stress tensor [13, 14]. Model Nos. 1–3 also include the differential transport equations for the kinetic turbulence energy $E = \langle u_i u^i \rangle/2$ and its dissipation rate ε. We note that the "standard" E–ε model of turbulence with the isotropic coefficient of turbulent viscosity is not capable of reproducing [9] the necessary anisotropy of the stress-tensor components $\langle u_i u_j \rangle$ without an additional modification of a speculative character.

Model Nos. 1–3 are formulated based on the model of second-order moments that was developed in [10, 11]. The suppression of the turbulent fluctuating characteristics as the flow swirling increases was taken into account by introducing an extra term with the Richardson swirling number into the equation for ε [9, 15, 16]. The damping effect of the wall on the transverse velocity fluctuations was described using the correction [12, 13] of the standard model for the pressure–velocity shear correlation in the equations which determine the second-order moments. To take into account the wall effects, the destruction terms in the equations for $\langle u_i u_j \rangle$ and ε were also modified in model Nos. 1–3 [14]. As the calculation results show, the three models adequately describe both the effect of the flow swirling on the turbulent momentum transfer and the effect of the solid wall. The difference between the models is, however, manifested in the accuracy of the numerical results obtained when the latter are compared with experimental data.

• *Governing Equations of the Model.* To describe the flow in a rotating pipe, we use a cylindrical coordinate system $x^i = (x, r, \varphi)$, where x is counted off along the pipe axis, r in the radial direction, and φ in the azimuthal direction. The tensor notation is used for an arbitrary curvilinear system of coordinates. In the cylindrical coordinates, the components of the mean and fluctuating velocity have the following form: $U_i = (U, V, rW)$, $U^i = (U, V, W/r)$, $u_i = (u, v, rw)$, and $u^i = (u, v, w/r)$. The system of exact (unclosed) transport equations for the mean velocity vector and the turbulent stress tensor for a steady incompressible flow is written in the general tensor notation:

$$U^i_{,i} = 0, \quad U^j U_{i,j} = \nu g^{jk} U_{i,jk} - \langle u_i u^j \rangle_{,j} - \hat{P}_{,i}/\rho; \tag{1}$$

$$U^k\langle u_iu_j\rangle_{,k} = \nu(g^{km}\langle u_iu_j\rangle_{,k})_{,m} + D_{ij} + P_{ij} + \Pi_{ij} - \varepsilon_{ij}, \tag{2}$$

where $D_{ij} = -\langle u_iu_ju^m\rangle_{,m} - (\langle pu_i\rangle_{,j} + \langle pu_j\rangle_{,i})/\rho$ (turbulent transfer), $P_{ij} = -\langle u_ju^k\rangle U_{i,k} - \langle u_iu^k\rangle U_{j,k}$ (the production of turbulence), $\Pi_{ij} = \langle p(u_{i,j} + u_{j,i})\rangle/\rho$ (the pressure–velocity shear correlation), $\varepsilon_{ij} = 2\nu g^{km}\langle u_{i,m}u_{j,k}\rangle$ (the dissipation), the subscript "$,i$" denotes the covariant differentiation with respect to the coordinate x^i, g^{ij} is the metric tensor, $\langle\cdots\rangle$ denotes the averaging in time, $\hat{P}$ is the mean pressure, p is the pressure fluctuation, ρ is the density, and ν is the kinematic viscosity.

To obtain the closed form of system (1) and (2), we need model representations for the terms D_{ij}, Π_{ij}, and ε_{ij}. The simplest model expression of gradient type for turbulent diffusion (third-order moments) processes is [17]

$$-\langle u_iu_ju^m\rangle = -g^{km}\langle u_iu_ju_k\rangle = g^{km}C_s\frac{E}{\varepsilon}\langle u_ku^\alpha\rangle\langle u_iu_j\rangle_{,\alpha}, \tag{3}$$

where $C_s = 0.18$ is an empirical coefficient. Along with the turbulence production $P = -(1/2)(\langle u_iu^k\rangle U^i_{,k} + \langle u^iu^k\rangle U_{i,k})$, the dissipation ε enters the equation for turbulence energy derived from (2) and (3):

$$U^kE_{,k} = \left[g^{km}\left(\nu E_{,k} + C_s\frac{E}{\varepsilon}\langle u_ku^\alpha\rangle E_{,\alpha}\right)\right]_{,m} + P - \varepsilon - \frac{2\nu E}{x_n^2}. \tag{4}$$

The last term in (4) appears in correcting the standard model relationship for $\varepsilon_{ij} = (2/3)\delta_{ij}\varepsilon$, which takes into account the effect of low Reynolds numbers [14] near the wall:

$$\varepsilon_{ij} = \frac{2}{3}g_{ij}\varepsilon + 2\nu\frac{\langle u_iu_j\rangle}{x_n^2} \tag{5}$$

(x_n is the distance from the wall).

The pressure–velocity shear correlation is simulated [11] as a sum of three terms:

$$\Pi_{ij} = \Pi_{ij}^{(1)} + \Pi_{ij}^{(2)} + \left(\Pi_{ij}^{\prime(1)} + \Pi_{ij}^{\prime(2)}\right)f(x_n). \tag{6}$$

The first term describes the tendency of turbulence to isotropy in the absence of the mean velocity shear and the wall effects:

$$\Pi_{ij}^{(1)} = -C_1\frac{\varepsilon}{E}\left(\langle u_iu_j\rangle - \frac{2}{3}g_{ij}E\right); \tag{7}$$

the second one describes the contribution of the mean-velocity gradients:

$$\Pi_{ij}^{(2)} = -C_2\left(P_{ij} - \frac{2}{3}g_{ij}P\right); \tag{8}$$

and the third term describes the wall effect [13]:

$$\Pi_{ij}^{\prime(1)} = C_1'\frac{\varepsilon}{E}\left[\langle u_n^2\rangle g_{ij} - \frac{3}{2}(\langle u_nu_j\rangle g_{in} + \langle u_nu_i\rangle g_{jn})\right]; \tag{9}$$

$$\Pi_{ij}^{\prime(2)} = C_2'\left[\Pi_{nn}^{(2)}g_{ij} - \frac{3}{2}(\Pi_{nj}^{(2)}g_{in} + \Pi_{ni}^{(2)}g_{jn})\right], \tag{10}$$

where the damping function is $f = (1/5)E^{3/2}/(\varepsilon x_n)$ [12] (the subscript n denotes the normal direction to the wall).

The value of ε in the model relationships is determined from the differential transport equation

$$U^k\varepsilon_{,k} = \left[g^{km}\left(\nu\varepsilon_{,k} + C_\varepsilon\frac{E}{\varepsilon}\langle u_ku^\alpha\rangle\varepsilon_{,\alpha}\right)\right]_{,m} + \left(C_{\varepsilon1}P - C_{\varepsilon2}^*\varepsilon\right)\frac{\varepsilon}{E} - \frac{2\nu\varepsilon}{x_n^2}f_1. \tag{11}$$

Here

$$f_1 = \exp(-0.5x_nu_*/\nu); \quad C_\varepsilon = 0.18; \quad C_{\varepsilon1} = 1.35; \quad C_{\varepsilon2} = 1.8;$$

$$C_{\varepsilon2}^* = \max[1.4; C_{\varepsilon2}f_2(1 - C_{\varepsilon3}\mathrm{Ri}_W)]; \quad f_2 = 1 - (2/9)\exp[-(E^2/(6\nu\varepsilon))^2];$$

$$\mathrm{Ri}_W = \left[\frac{W}{r}\frac{\partial W}{\partial r}\right] \Big/ \left[\left(\frac{\partial U}{\partial r}\right)^2 + \left(\frac{\partial W}{\partial r}\right)^2\right].$$

The Richardson swirling number Ri_W (11) is introduced to describe the influence of the streamline curvature similarly to the influence of the medium's stratification on the turbulent transfer [15]. The correction for the streamline curvature is included in the destruction term in (11) according to [16]. The expression for Ri_W is taken in a more general form than in [16] by analogy with the Richardson number in stratified turbulent flows [9, 13]. The correction of destruction in Eq. (11) is based on the hypothesis that the stabilizing effect of swirling can be simulated by decreasing the length scale of turbulent vortices $L = E^{3/2}/\varepsilon$ for $\mathrm{Ri}_W > 0$ (i.e., owing to an increase in the dissipation ε leading to the suppression of the turbulence energy E). The coefficient $C^*_{\varepsilon 2}$ is limited from below ($C^*_{\varepsilon 2} \geqslant 1.4$) so that the dissipation ε does not become "too large" on account of the excessive decrease in the coefficient $C_{\varepsilon 2} f_2 (1 - C_{\varepsilon 3}\mathrm{Ri}_W)$ with an increase in Ri_W as the swirling parameter increases (SP > 0.6).

• *Model No. 1 for an Axisymmetric Flow in a Pipe.* The model representations formulated above lead to a closed system of turbulent transport equations for the first- and second-order moments. For a steady axisymmetric flow in a pipe, the governing equations of the model in the cylindrical coordinate system have the form

$$\frac{\partial U}{\partial x} + \frac{1}{r}\frac{\partial}{\partial r}(rV) = 0; \tag{12}$$

$$U\frac{\partial U}{\partial x} + V\frac{\partial U}{\partial r} = \frac{1}{r}\frac{\partial}{\partial r}\left[r\left(\nu\frac{\partial U}{\partial r} - \langle uv\rangle\right)\right] - \frac{1}{\rho}\frac{\partial \hat{P}}{\partial x}; \tag{13}$$

$$U\frac{\partial W}{\partial x} + V\frac{\partial W}{\partial r} + V\frac{W}{r} = \frac{1}{r}\frac{\partial}{\partial r}\left[r\left(\nu\frac{\partial W}{\partial r} - \langle vw\rangle\right)\right] - \nu\frac{W}{r^2} - \frac{\langle vw\rangle}{r}; \tag{14}$$

$$U\frac{\partial E}{\partial x} + V\frac{\partial E}{\partial r} = \frac{1}{r}\frac{\partial}{\partial r}\left[r\left(\nu + C_s\frac{E}{\varepsilon}\langle v^2\rangle\right)\frac{\partial E}{\partial r}\right] + P - \varepsilon - \frac{2\nu E}{(R-r)^2}; \tag{15}$$

$$U\frac{\partial \varepsilon}{\partial x} + V\frac{\partial \varepsilon}{\partial r} = \frac{1}{r}\frac{\partial}{\partial r}\left[r\left(\nu + C_\varepsilon\frac{E}{\varepsilon}\langle v^2\rangle\right)\frac{\partial \varepsilon}{\partial r}\right] + \{C_{\varepsilon 1}P - C^*_{\varepsilon 2}\varepsilon\}(\varepsilon/E) - \frac{2\nu\varepsilon}{(R-r)^2}f_1, \tag{16}$$

where U, V, and W are the components of the mean velocity vector in the longitudinal, radial, and azimuthal directions, and u, v, and w are the corresponding fluctuating velocity components. The turbulent stresses in (13)–(16) are found from the differential transport equations (2), which were closed according to (3) and (5)–(10). For individual components of the stress tensor, these equations are written as

$$U\frac{\partial\langle u^2\rangle}{\partial x} + V\frac{\partial\langle u^2\rangle}{\partial r} = \frac{1}{r}\frac{\partial}{\partial r}\left[r\left(\nu + C_s\frac{E}{\varepsilon}\langle v^2\rangle\right)\frac{\partial\langle u^2\rangle}{\partial r}\right] + P_{uu}$$
$$+\left\{-C_1\frac{\varepsilon}{E}\left(\langle u^2\rangle - \frac{2}{3}E\right) - C_2\left(P_{uu} - \frac{2}{3}P\right) + \Pi' f\right\} - \frac{2}{3}\varepsilon - \frac{2\nu}{(R-r)^2}\langle u^2\rangle; \tag{17}$$

$$U\frac{\partial\langle v^2\rangle}{\partial x} + V\frac{\partial\langle v^2\rangle}{\partial r} - 2\langle vw\rangle\frac{W}{r} = \frac{1}{r}\frac{\partial}{\partial r}\left[r\left(\nu + C_s\frac{E}{\varepsilon}\langle v^2\rangle\right)\frac{\partial\langle v^2\rangle}{\partial r}\right]$$
$$-\frac{2}{r}C_s\left[\frac{\partial}{\partial r}\left(\frac{E}{\varepsilon}\langle vw\rangle\langle vw\rangle\right) + \frac{E}{\varepsilon}\langle vw\rangle\frac{\partial\langle vw\rangle}{\partial r}\right] + 2\left(\nu + C_s\frac{E}{\varepsilon}\langle w^2\rangle\right)\frac{\langle w^2\rangle - \langle v^2\rangle}{r^2} + P_{vv}$$
$$+\left\{-C_1\frac{\varepsilon}{E}\left(\langle v^2\rangle - \frac{2}{3}E\right) - C_2\left(P_{vv} - \frac{2}{3}P\right) - 2\Pi' f\right\} - \frac{2}{3}\varepsilon - \frac{2\nu}{(R-r)^2}\langle v^2\rangle; \tag{18}$$

$$U\frac{\partial\langle w^2\rangle}{\partial x} + V\frac{\partial\langle w^2\rangle}{\partial r} + 2\langle vw\rangle\frac{W}{r} = \frac{1}{r}\frac{\partial}{\partial r}\left[r\left(\nu + C_s\frac{E}{\varepsilon}\langle v^2\rangle\right)\frac{\partial\langle w^2\rangle}{\partial r}\right]$$
$$+\frac{2}{r}C_s\left[\frac{\partial}{\partial r}\left(\frac{E}{\varepsilon}\langle vw\rangle\langle vw\rangle\right) + \frac{E}{\varepsilon}\langle vw\rangle\frac{\partial\langle vw\rangle}{\partial r}\right] - 2\left(\nu + C_s\frac{E}{\varepsilon}\langle w^2\rangle\right)\frac{\langle w^2\rangle - \langle v^2\rangle}{r^2} + P_{ww}$$

$$+\Big\{-C_1\frac{\varepsilon}{E}\Big(\langle w^2\rangle-\frac{2}{3}E\Big)-C_2\Big(P_{ww}-\frac{2}{3}P\Big)+\Pi' f\Big\}-\frac{2}{3}\varepsilon-\frac{2\nu}{(R-r)^2}\langle w^2\rangle$$

$$\Big(\Pi'=C_1'\frac{\varepsilon}{E}\langle v^2\rangle-C_2'C_2\Big(P_{vv}-\frac{2}{3}P\Big),\quad f=\frac{1}{5}\frac{E^{3/2}}{(R-r)\varepsilon}\Big); \tag{19}$$

$$U\frac{\partial\langle uv\rangle}{\partial x}+V\frac{\partial\langle uv\rangle}{\partial r}-\langle uw\rangle\frac{W}{r}=\frac{1}{r}\frac{\partial}{\partial r}\Big[r\Big(\nu+C_s\frac{E}{\varepsilon}\langle v^2\rangle\Big)\frac{\partial\langle uv\rangle}{\partial r}\Big]$$

$$-\frac{C_s}{r}\Big[\frac{\partial}{\partial r}\Big(\frac{E}{\varepsilon}\langle vw\rangle\langle uw\rangle\Big)+\frac{E}{\varepsilon}\langle vw\rangle\frac{\partial\langle uw\rangle}{\partial r}\Big]-\Big(\nu+C_s\frac{E}{\varepsilon}\langle w^2\rangle\Big)\frac{\langle uv\rangle}{r^2}+P_{uv}$$

$$+\Big\{-C_1\frac{\varepsilon}{E}\langle uv\rangle-C_2P_{uv}-\frac{3}{2}\Big(C_1'\frac{\varepsilon}{E}\langle uv\rangle+C_2'C_2P_{uv}\Big)f\Big\}-\frac{2\nu}{(R-r)^2}\langle uv\rangle; \tag{20}$$

$$U\frac{\partial\langle vw\rangle}{\partial x}+V\frac{\partial\langle vw\rangle}{\partial r}-[\langle w^2\rangle-\langle v^2\rangle]\frac{W}{r}=\frac{1}{r}\frac{\partial}{\partial r}\Big[r\Big(\nu+C_s\frac{E}{\varepsilon}\langle v^2\rangle\Big)\frac{\partial\langle vw\rangle}{\partial r}\Big]$$

$$-\frac{C_s}{r}\Big[\frac{\partial}{\partial r}\Big(\frac{E}{\varepsilon}\langle vw\rangle(\langle w^2\rangle-\langle v^2\rangle)\Big)+\frac{E}{\varepsilon}\langle vw\rangle\frac{\partial}{\partial r}(\langle w^2\rangle-\langle v^2\rangle)\Big]-4\Big(\nu+C_s\frac{E}{\varepsilon}\langle w^2\rangle\Big)\frac{\langle vw\rangle}{r^2}+P_{vw}$$

$$+\Big\{-C_1\frac{\varepsilon}{E}\langle vw\rangle-C_2P_{vw}-\frac{3}{2}\Big(C_1'\frac{\varepsilon}{E}\langle vw\rangle+C_2'C_2P_{vw}\Big)f\Big\}-\frac{2\nu}{(R-r)^2}\langle vw\rangle; \tag{21}$$

$$U\frac{\partial\langle uw\rangle}{\partial x}+V\frac{\partial\langle uw\rangle}{\partial r}+\langle uv\rangle\frac{W}{r}=\frac{1}{r}\frac{\partial}{\partial r}\Big[r\Big(\nu+C_s\frac{E}{\varepsilon}\langle v^2\rangle\Big)\frac{\partial\langle uw\rangle}{\partial r}\Big]$$

$$+\frac{C_s}{r}\Big[\frac{\partial}{\partial r}\Big(\frac{E}{\varepsilon}\langle vw\rangle\langle uv\rangle\Big)+\frac{E}{\varepsilon}\langle vw\rangle\frac{\partial\langle uv\rangle}{\partial r}\Big]-\Big(\nu+C_s\frac{E}{\varepsilon}\langle w^2\rangle\Big)\frac{\langle uw\rangle}{r^2}$$

$$+P_{uw}+\Big\{-C_1\frac{\varepsilon}{E}\langle uw\rangle-C_2P_{uw}\Big\}-\frac{2\nu}{(R-r)^2}\langle uw\rangle. \tag{22}$$

$$P_{uu}=-2\langle uv\rangle\frac{\partial U}{\partial r},\quad P_{vv}=2\langle vw\rangle\frac{W}{r},\quad P_{ww}=-2\langle vw\rangle\frac{\partial W}{\partial r},$$

The terms of turbulence production in (17)–(22) have the form

$$P_{uu}=-2\langle uv\rangle\frac{\partial U}{\partial r},\quad P_{vv}=2\langle vw\rangle\frac{W}{r},\quad P_{ww}=-2\langle vw\rangle\frac{\partial W}{\partial r},$$

$$P_{uv}=-\langle v^2\rangle\frac{\partial U}{\partial r}+\langle uw\rangle\frac{W}{r},\quad P_{vw}=-\langle v^2\rangle\frac{\partial W}{\partial r}+\langle w^2\rangle\frac{W}{r},$$

$$P_{uw}=-\langle uv\rangle\frac{\partial W}{\partial r}-\langle vw\rangle\frac{\partial U}{\partial r},\quad P=\frac{1}{2}(P_{uu}+P_{vv}+P_{ww}).$$

For convenience of numerical realization, instead of Eqs. (18) and (19) for $\langle v^2\rangle$ and $\langle w^2\rangle$, we used Eq. (15) for $E=(1/2)(\langle u^2\rangle+\langle v^2\rangle+\langle w^2\rangle)$ and the equation for $a=\langle w^2\rangle-\langle v^2\rangle$ obtained from (18) and (19). The latter substitution is due to the presence of a singularity at the pipe axis in the equations for $\langle v^2\rangle$ and $\langle w^2\rangle$, which is caused by a source of the form $\pm2(\nu+C_s(E/\varepsilon)\langle w^2\rangle)(a/r^2)$ if $a\neq0$. The values of $\langle v^2\rangle$ and $\langle w^2\rangle$ are determined from the values of E, $\langle u^2\rangle$, and a found from the transport equations: $\langle v^2\rangle=E-(\langle u^2\rangle+a)/2$ and $\langle w^2\rangle=a+\langle v^2\rangle$. The pressure gradient $-(1/\rho)(\partial\hat{P}/\partial x)$ in (13) can be determined by integrating (13) in the small-convection approximation $U(\partial U/\partial x)+V(\partial U/\partial r)$ (the numerical experiments supported this assumption). The integration of (13) over the pipe cross section yields

$$-\frac{1}{\rho}\frac{d\hat{P}}{dx}=\frac{2}{R^2}\Big[-r\Big(\nu\frac{\partial U}{\partial r}-\langle uv\rangle\Big)\Big|_0^R\Big]=\frac{2\nu}{R}\Big(-\frac{\partial U}{\partial r}\Big)_{r=R},$$

whence we find the friction velocity on the wall $u_*=[\nu(-\partial U/\partial r)_{r=R}]^{1/2}$ which enters the damping function f_1 in Eq. (16) for dissipation.

TABLE 1

Model	C_1	C_2	C_1'	C_2'	$C_{\varepsilon 1}$	$C_{\varepsilon 2}$	$C_{\varepsilon 3}$	C_ε	C_s
No. 1	1.5	0.6	0.3	0.3	1.35	1.8	2.0	0.18	0.18
Nos. 2 and 3	1.5	0.6	0.3	0.3	1.35	1.8	2.5	0.18	0.18

The values of the numerical coefficients for the model of the Reynolds-stress transport equations (model No. 1) are listed in Table 1. The same values were used in [9, 11–13].

Model with Algebraic Relationships for Reynolds Stresses. The differential transport equations (2) for turbulent stresses can be simplified to algebraic equations assuming the convection and diffusion terms to be small in comparison with turbulence production and dissipation, and also assuming the transfer of tensor components $\langle u_i u_j \rangle$ to be proportional to the transfer of turbulence energy [9]:

$$U^k \langle u_i u_j \rangle_{,k} - \nu (g^{km} \langle u_i u_j \rangle_{,k})_{,m} - D_{ij} = P_{ij} + \Pi_{ij} - \varepsilon_{ij} = \left(\frac{\langle u_i u_j \rangle}{E} \right) k \left[P - \varepsilon - \frac{2\nu E}{(R-r)^2} \right]. \tag{23}$$

The coefficient is $k = 0$ in the local-equilibrium approximation [13] and $k = 1$ in the nonequilibrium approximation [9, 12]. Having substituted the exact form of the turbulence production P_{ij} and the model approximations (5)–(10) for the correlations Π_{ij} and ε_{ij}, we find the sought second-order moments from (23). For an axisymmetric flow in a pipe, the relationships for the second-order moments are obtained by simplifying Eqs. (17)–(22) for individual components of the Reynolds stress tensor according to (23):

$$\langle u^2 \rangle = \frac{(2/3)[(C_1 - 1)\varepsilon + C_2 P] + (1 - C_2) P_{uu} + \Pi' f}{C_1 (\varepsilon / E) + 2\nu/(R-r)^2 + k[P - \varepsilon - 2\nu E/(R-r)^2]/E}; \tag{24}$$

$$\langle v^2 \rangle = \frac{\frac{2}{3}[(C_1 - 1)\varepsilon + C_2 P] + (1 - C_2) P_{vv} + 2C_2' C_2 (P_{vv} - \frac{2}{3} P) f + \frac{2\nu \langle w^2 \rangle}{r^2}}{(C_1 + 2C_1' f)\frac{\varepsilon}{E} + \frac{2\nu}{(R-r)^2} + \frac{2\nu}{r^2} + k\left[\frac{P - \varepsilon}{E} - \frac{2\nu}{(R-r)^2} \right]}; \tag{25}$$

$$\langle w^2 \rangle = \frac{\frac{2}{3}[(C_1 - 1)\varepsilon + C_2 P] + (1 - C_2) P_{ww} + \Pi' f + \frac{2\nu \langle v^2 \rangle}{r^2}}{C_1 \frac{\varepsilon}{E} + \frac{2\nu}{(R-r)^2} + \frac{2\nu}{r^2} + k\left[\frac{P - \varepsilon}{E} - \frac{2\nu}{(R-r)^2} \right]}; \tag{26}$$

$$\langle uv \rangle = \frac{(1 - C_2 - 3C_2' C_2 f/2) P_{uv}}{(C_1 + 3C_1' f/2)(\varepsilon/E) + 2\nu/(R-r)^2 + \nu/r^2} = A_{uv} P_{uv}; \tag{27}$$

$$\langle vw \rangle = \frac{(1 - C_2 - 3C_2' C_2 f/2) P_{vw}}{(C_1 + 3C_1' f/2)(\varepsilon/E) + 2\nu/(R-r)^2 + 4\nu/r^2} = A_{vw} P_{vw}; \tag{28}$$

$$\langle uw \rangle = \frac{(1 - C_2) P_{uw}}{C_1 (\varepsilon/E) + 2\nu/(R-r)^2 + \nu/r^2} = A_{uw} P_{uw}. \tag{29}$$

Note that a correction in the form of the terms added from the second component on the left-hand side of the governing equation (23) and proportional to ν/r^2 is introduced into (25)–(29). This correction is necessary to describe the correct behavior of not only the second-order moments ($r^2 \sim \langle w^2 \rangle - \langle v^2 \rangle \sim \langle vw \rangle \to 0$ at $r \to 0$) near the axis, but also the mean circumferential velocity ($W \sim r$ at $r \to 0$) at large swirling parameters. This correction can also be regarded as a "penalty" of the algebraic model (24)–(29), since the complete second-order closure model (12)–(22) automatically takes into account the asymptotic behavior of the sought quantities near the axis.

With allowance for (29), Eqs. (27) and (28) become

$$-\langle uv \rangle = \frac{\langle v^2 \rangle + A_{uw} \langle vw \rangle (W/r)}{A_{uv}^{-1} + A_{uw} (W/r)(\partial W / \partial r)} \frac{\partial U}{\partial r} = \nu_{tU} \frac{\partial U}{\partial r}; \tag{30}$$

$$-\langle vw\rangle = \nu_{tW}\frac{\partial W}{\partial r} - \alpha_{tW}\frac{W}{r}, \quad \nu_{tW} = A_{vw}\langle v^2\rangle, \quad \alpha_{tW} = A_{vw}\langle w^2\rangle, \tag{31}$$

in which the "effective coefficients of turbulent viscosity" ν_{tU}, ν_{tW}, and α_{tW} are complex functions of W, E, ε, and other parameters. With (30) and (31) taken into account, Eqs. (13) and (14) are reduced to the parabolic equations

$$U\frac{\partial U}{\partial x} + V\frac{\partial U}{\partial r} = \frac{1}{r}\frac{\partial}{\partial r}\left[r(\nu + \nu_{tU})\frac{\partial U}{\partial r}\right] - \frac{1}{\rho}\frac{\partial \hat{P}}{\partial x}; \tag{32}$$

$$U\frac{\partial W}{\partial x} + V\frac{\partial W}{\partial r} + V\frac{W}{r} = \frac{1}{r}\frac{\partial}{\partial r}\left[r(\nu + \nu_{tW})\frac{\partial W}{\partial r}\right] - \nu\frac{W}{r^2} - \frac{1}{r}\left[\frac{\partial(\alpha_{tW}W)}{\partial r} + \langle vw\rangle\right]. \tag{33}$$

Equations (12), (32), and (33) for the mean velocity field, (15) and (16) for the turbulence energy and its dissipation rate, and also relations (24)–(31) for turbulent stresses yield the model of turbulent transfer with algebraic relationships for the second-order moments. The coefficient in formulas (24)–(26) is $k = 1$ in the nonequilibrium approximation (model No. 2) and $k = 0$ in the local-equilibrium approximation (model No. 3). The empirical coefficients of model Nos. 2 and 3 are given in Table 1.

Numerical Implementation of Turbulence Models. The following boundary conditions are used for the differential transport equations in model Nos. 1–3:
for $r = 0$ (at the pipe axis), we have

$$\frac{\partial U}{\partial r} = \frac{\partial E}{\partial r} = \frac{\partial \varepsilon}{\partial r} = \frac{\partial\langle u^2\rangle}{\partial r} = \frac{\partial a}{\partial r} = \langle uv\rangle = \langle vw\rangle = \langle uw\rangle = W = 0$$

and, for $r = R$ (at the wall), we have

$$U = E = \varepsilon = \langle u^2\rangle = a = \langle uv\rangle = \langle vw\rangle = \langle uw\rangle = 0, \quad W = W_0 > 0.$$

The governing system of parabolic type for U, W, E, ε (and for $\langle u_i u_j\rangle$ in model No. 1) is solved by the control-volume method [18]. The transport equations for the sought quantities F are written in the Mises variables (the coordinate x is the stream function ψ) in the general form:

$$\left(\frac{\partial F}{\partial x}\right)_{\psi} = \frac{\partial}{\partial \psi}\left[r^2 U\Gamma_F\frac{\partial F}{\partial \psi}\right] + \frac{S_F}{U}, \tag{34}$$

where Γ_F is the diffusion coefficient and S_F is the source term.

The computational domain was split in the transverse direction into $N - 1$ intervals. The procedure of numerical solution of equations of the form (34) is a noniterative process of step-by-step integration. It was described in detail by Spalding [18]. The step Δx of integration with respect to the coordinate x and the number of points $N = 128$ were chosen from the condition of retention of the necessary accuracy of calculations (variation of the sought quantities within 1% of their maximum values with a twofold decrease in Δx or a twofold increase in N). The grid is nonuniform in the r direction:

(a) $\Delta r_i = \nu/u_{*0}$ for $0 \leqslant y^+ \leqslant 5$ (10 equal intervals in the viscous sublayer) and u_{*0} is the friction velocity on the wall in the exit cross section of the nonrotating section of the pipe;

(b) $\Delta r_{i+1} = \beta\Delta r_i$ for $5 < y^+ \leqslant 50$ (an increase of the intervals in a geometrical progression from the pipe wall in the transient region);

(c) $\Delta r_i = \text{const} \gg \nu/u_{*0}$ for $50 < y^+ \leqslant \text{Re}^*$, where $y^+ = (R - r)u_{*0}/\nu = (1 - r/R)\text{Re}^*$ (100 equal intervals in the external flow up to the wind-tunnel axis).

The flow-rate conservation law in the variables (x, ψ) was fulfilled automatically:

$$\int_0^R Ur\,dr = \psi(R) - \psi(0) = \text{const},$$

since the condition

$$\psi(r_{i+1}) - \psi(r_i) = \int_{r_i}^{r_{i+1}} Ur\,dr = \text{const}, \qquad i = 1, \ldots, N - 1,$$

holds on each interval in integrating over the control volumes. The values of r_i were calculated using the recurrent formula

$$r_{i+1}^2 - r_i^2 = 2 \int_{\psi(r_i)}^{\psi(r_{i+1})} \frac{d\psi}{U}.$$

The condition $r_N = R$, i.e.,

$$\sum_{i=1}^{N-1} \int_{\psi(r_i)}^{\psi(r_{i+1})} \frac{d\psi}{U} = \frac{R^2}{2},$$

was satisfied by multiplying the velocity U at all points by the residual $(r_N^2 - r_1^2)/R^2$ in each cross section $x = \text{const}$.

The calculation was performed in two stages: (1) obtaining a developed flow without swirling; (2) superposition of the pipe rotation with velocity $W_0 = \omega R$ onto the developed flow.

At the first stage of computations, the initial velocity profile was prescribed as a combination of the linear [$U(r) = u_* y^+$ for $0 < y^+ \leqslant y_R^+$] and power [$U(r) = C_t u_* (y^+)^{1/7}$, where $C_t = 8.74$ and $y_R^+ = C_t^{7/6}$, for $y_R^+ < y^+ \leqslant \mathrm{Re}^*$] functions. The turbulence energy and its components were chosen equal to the small background values: $E(r) = E_0 = 10^{-3} u_{*0}^2$, $\langle u^2 \rangle = (2/3)E_0$, and $a = 0$; the shear stress was $\langle uv \rangle\big|_{x=0} = 0$. Assuming the local equilibrium ($P = \varepsilon$) and the gradient relationship $\langle uv \rangle = -C_\mu f_\mu (E^2/\varepsilon)(\partial U/\partial r)$ (the value of $C_\mu = 0.09$ and the damping function $f_\mu = 1 - \exp(-0.01\, y^+)$ are borrowed from [14]), we found the turbulence energy dissipation: $\varepsilon(r) = \sqrt{C_\mu f_\mu}\, E_0 |\partial U/\partial r|$.

At the second stage, the initial data were the transverse profiles of U, E, ε, $\langle uv \rangle$, $\langle u^2 \rangle$, and $a = \langle w^2 \rangle - \langle v^2 \rangle$ obtained at the first stage, forming a developed turbulent flow in a pipe. The remaining functions to be found were $W(r = R) = W_0$ and $W(r < R) = \langle vw \rangle = \langle uw \rangle = 0$.

The calculated characteristics were normalized by the dynamic velocity u_{*0} and the pipe radius R. The input parameter $\mathrm{Re}^* = R u_{*0}/\nu = 875$ was the same as in the experiment ($R = 3$ cm, $U_0 = 10^3$ cm/sec, $\nu = 0.149$ cm^2/sec, and $u_{*0} = 43.5$ cm/sec). A distance of $200R$ along the x coordinate along the pipe axis was covered at the first stage of calculations, and this distance was $50R$ at the second stage, as in the experiment. Flow stabilization with an increase in x can be characterized by the value of advection of the turbulence energy, which decreases at the end of the first stage to a negligible value:

$$\left| U(\partial E/\partial x)_\psi \right|_{\max} \sim 10^{-2}(u_{*0}^3/R) \ll \varepsilon_{\min}.$$

The relative value of advection was significantly larger at the end of the second stage, and stabilization of the turbulent flow characteristics along x was not observed.

Results of Laboratory and Numerical Experiments. Verification of the Accuracy of the Turbulent Transport Models. Results of laboratory and numerical experiments for a flow in a rotating pipe with different swirling parameters are presented in Figs. 1–5 (for the exit cross section of the rotated section of the pipe for $x/R = 50$).

In a nonswirling flow, the measured results of the longitudinal component of the mean velocity, Reynolds stress, turbulence energy, and its dissipation rate are in reasonable agreement with the known data [19–22]. The experimental profile $U(r)/U_0$ for SP = 0 is approximately described by a power (logarithmic) law (Fig. 1a). The difference of the $U(r)$ profiles at the pipe axis calculated by the three models does not exceed 2% for a nonswirling flow and approximately 5% for a swirling flow. Figure 1a shows the profile $U(r)$ obtained using model No. 1 for the second-order moments, which is in better agreement with the experimental data for a swirling flow than the profiles found using model Nos. 2 and 3 with algebraic relationships for the second-order moments (not shown in Fig. 1a); for SP > 0, the data are shown in the exit cross section of the rotated section of the pipe ($x/R = 50$).

The measurement results for dissipation $\varepsilon(r)$ (Fig. 2b) for SP = 0 are readily reproduced by model Nos. 1–3 in the region $0 < r/R < 0.5$. There is not much difference between the calculated dissipation profiles for the three models and, therefore, only the profiles obtained using model No. 1 of the second-order

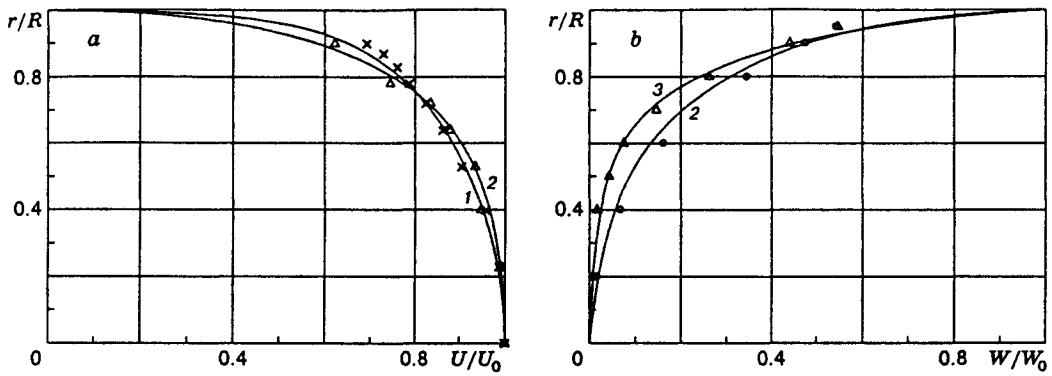

Fig. 1. Profiles of the longitudinal U/U_0 (a) and circumferential W/W_0 (b) components of the mean velocity for various SP values: curves 1–3 refer to the calculation using the differential model No. 1; points ×, △, and ○ refer to the experimental data [5–8]; SP = 0 (curve 1 and the point ×), 0.6 (curve 2 and the point △), and 0.15 (curve 3 and the point ○).

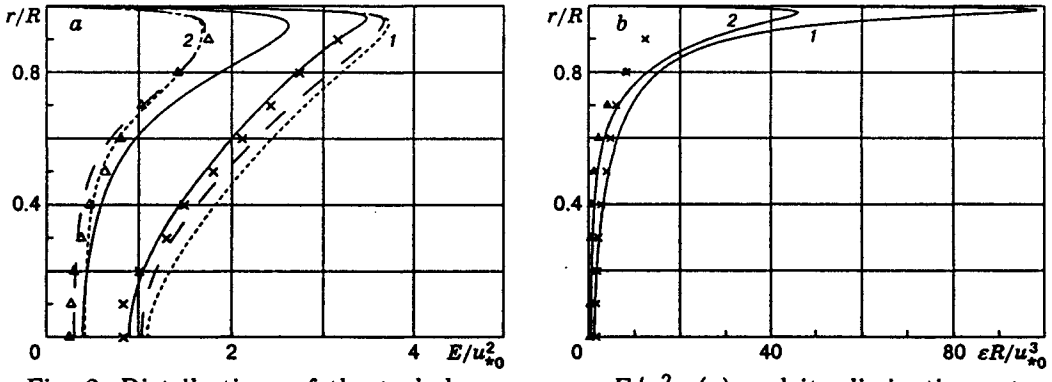

Fig. 2. Distributions of the turbulence energy E/u_{*0}^2 (a) and its dissipation rate $\varepsilon R/u_{*0}^3$ (b): the solid, dashed, and dotted curves refer to the calculations using model Nos. 1, 2, and 3, respectively; see also the legend in Fig. 1.

moments are shown in Fig. 2b. Model No. 1 is the best for the reproduction of the profile of turbulence energy E/u_{*0}^2, and model No. 3 is less suitable for this purpose (Fig. 2a). Model No. 1 more adequately describes the turbulent stress-tensor components (Fig. 3), in particular, the experimentally observed anisotropy of the normal stresses both near the wall and at the flow axis, where $\langle v^2\rangle = \langle w^2\rangle$ and $\langle u^2\rangle \simeq 2\langle v^2\rangle$. The locally equilibrium model No. 3 yields the worst agreement for the shear and normal stresses, in particular, at the pipe axis ($\langle u^2\rangle \approx \langle v^2\rangle \approx \langle w^2\rangle$).

As the flow swirling increases, with constant air flow rate, an increase in the longitudinal component of the mean velocity near the flow axis (for $0 < \mathrm{SP} \leqslant 0.6$) is observed both in calculations and experiments (Fig. 1a). The deformation of the profile $U(r)$ is caused by the curving of the streamlines in the radial direction under the action of the centrifugal force: they crowd together near the wall and are less compact near the axis. The profile $\partial U/\partial r$ becomes more shallow near the wall, which points to a decrease in the turbulent friction as the degree of swirling increases. Our experimental data were obtained for one velocity at the axis. The calculations were performed for a constant flow rate. The behavior of the curves $U(r)/U_0$ in Fig. 1a shows that the character of the swirling effect is identical in calculations and experiments.

As the rotation frequency of the pipe increases, the relative value of the circumferential component of the mean velocity in the axial region decreases (Fig. 1b). Thus, the distribution of $W(r)/W_0$ over the radius becomes increasingly nonuniform with increasing degree of swirling (this is shown in the exit cross section of

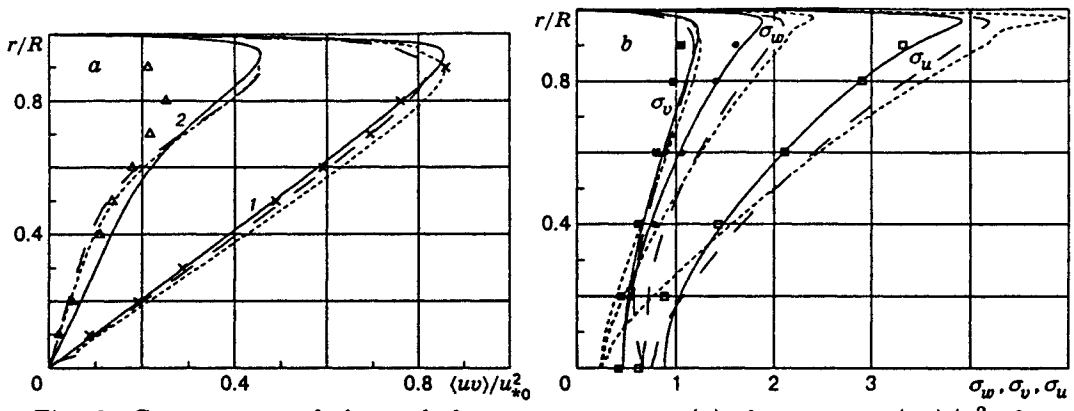

Fig. 3. Components of the turbulent stress tensor: (a) shear stress $\langle uv\rangle/u_{*0}^2$ for SP = 0 and 0.6; (b) normal stress for SP = 0; the experimental points □, ■, and • correspond to $\sigma_u = \langle u^2\rangle/u_{*0}^2$, $\sigma_v = \langle v^2\rangle/u_{*0}^2$, and $\sigma_w = \langle w^2\rangle/u_{*0}^2$; see also the legend in Figs. 1 and 2.

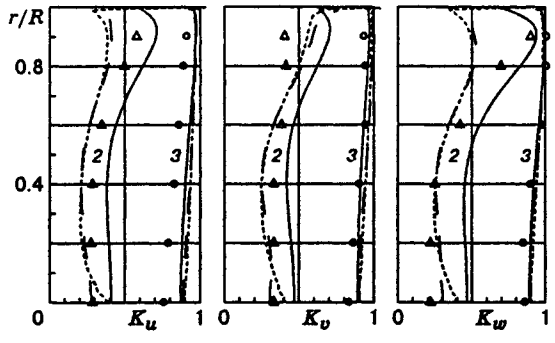

Fig. 4

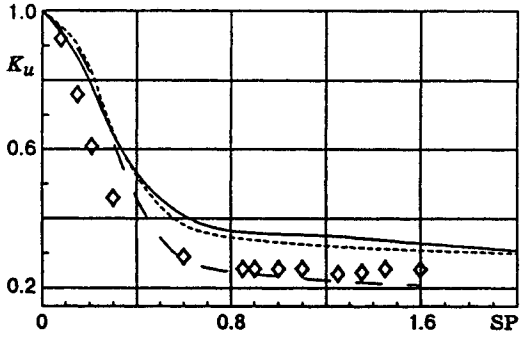

Fig. 5

Fig. 4. Transverse profiles of the "damping coefficients" $K_u = \langle u^2\rangle(\mathrm{SP} > 0)/\langle u^2\rangle(\mathrm{SP} = 0)$, $K_v = \langle v^2\rangle(\mathrm{SP} > 0)/\langle v^2\rangle(\mathrm{SP} = 0)$, and $K_w = \langle w^2\rangle(\mathrm{SP} > 0)/\langle w^2\rangle(\mathrm{SP} = 0)$ (see the legend in Figs. 1 and 2).

Fig. 5. Longitudinal "damping coefficient" K_u versus the swirling parameter $\mathrm{SP} = W_0/U_0$ for $r/R = 0$ and $x/R = 50$: see the legend for the curves in Figs. 1 and 2; the points ◇ refer to experimental data.

the rotated section of the pipe). Model No. 1 of the second-order moments adequately describes W/W_0 for SP = 0.15 and 0.6. The values of the circumferential velocity $W(r)/W_0$ calculated using model Nos. 2 and 3 are significantly larger than the measured values for all the SP > 0 (they are not shown in Fig. 1b).

The three models of turbulence reproduce the experimentally observed effect of the decrease in the fluctuating characteristics E, ε, and $\langle u_i u_j\rangle$ as the swirling parameter increases (Figs. 2–6). The anisotropy of the turbulence-energy components observed in a nonswirling flow (Fig. 3b) is also retained in the presence of flow swirling both in experiment and in calculations by model Nos. 1–3. The influence of the swirling on the components of the normal stresses $\langle u_\alpha^2\rangle$ was evaluated using the "damping coefficient" (no summation over the subscript was performed)

$$K_\alpha = \langle u_\alpha^2\rangle(\mathrm{SP} > 0)/\langle u_\alpha^2\rangle(\mathrm{SP} = 0)$$

for the α-th root-mean-square velocity fluctuations. For weak swirling (SP $\leqslant$ 0.3), the most profound suppression of the fluctuation intensity was observed at the flow axis. As the swirling increases (SP > 0.6),

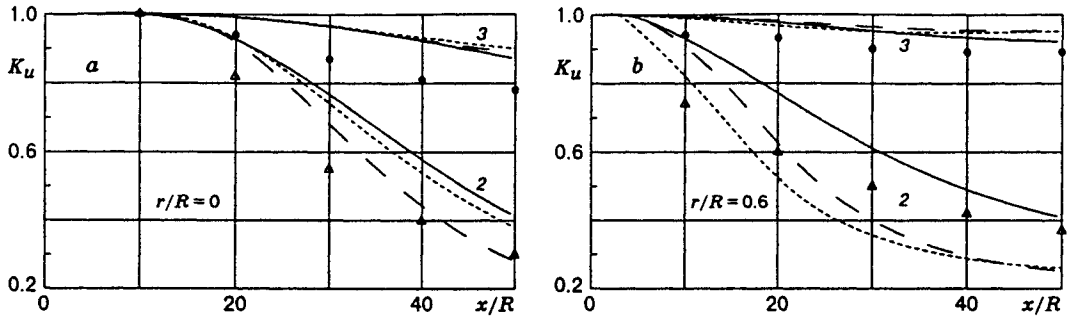

Fig. 6. Variation of K_u with increasing relative coordinate x/R counted off from the beginning of the rotated section: at the pipe axis ($r = 0$) (a) and for $r/R = 0.6$ (b); see the legend in Figs. 1 and 2.

the maximum of suppression shifts to the region $0.3 < r/R < 0.6$. Model Nos. 1–3 reproduce these effects (Fig. 4). On the whole, the differential model No. 1 of the second-order moments better describes the behavior of the "damping coefficients" for SP = 0.15 and 0.6.

The curves of the "damping coefficient" K_u versus the swirling parameter SP, which were calculated using model Nos. 1–3, are in reasonable agreement with experimental data (Fig. 5). The behavior of the calculated curves is characterized, as in experiment, by the terminated suppression of the intensity of turbulent fluctuations for SP > 0.85 (the effect of saturation with respect to the swirling parameter).

The marching procedure of step-by-step integration over control volumes, which was used for numerical simulation, makes it possible to trace the changes in the flow characteristics with increasing longitudinal coordinate x. As x increases, the "damping coefficient" demonstrates the same behavior as in the experiment (Fig. 6). For $r/R = 0.6$, the swirling effect is manifested more significantly, and it is observed at a distance of $x/R \simeq 4$–5 from the beginning of the rotated section and at a distance of $x/R \simeq 10$–14 at the pipe axis. Thus, the flow does not experience the swirling effect in a converging cone at the beginning of the rotated section of the pipe. The results of model No. 2 and No. 1 are close to the experimental results obtained, respectively, at the pipe axis (Fig. 6a) and outside the axial region (Fig. 6b).

Conclusions. The results of an experimental study and mathematical simulation of a developed turbulent flow in a straight round pipe rotated about its longitudinal axis show that flow swirling leads to significant changes in its characteristics: for insignificant and moderate degrees of swirling, the turbulent exchange processes are suppressed, i.e., the turbulent shear stresses, three components of the turbulence energy, and its dissipation rate decrease. The flow parameters change throughout the length of the rotated section (here $0 < x/R < 50$), and a pattern that is independent of a further increase in the distance from the beginning of the section along the x axis is not obtained. On the whole, the model of the transport equations for the Reynolds stress (model No. 1) gives better agreement with experimental data than the models with algebraic relationships for the second-order moments (model Nos. 2 and 3). Model No. 2 with nonequilibrium relationships for normal stresses allows, in turn, a more exact calculation of the behavior of the turbulence energy and its components in the axial flow region with a moderate velocity of pipe rotation than model No. 3.

This work was supported by the Russian Foundation for Fundamental Research (Grant Nos. 93-013-17632, 94-05-16287, 96-15-96310, and 96-02-16001) and INTAS (Grant No. 93-2492-ext and ICFPM program).

REFERENCES

1. L. Prandtl, "Einfluss stabilisierender Krafte auf die Turbulenz," in: *Vortrage aus d. Gtd. d. Aerodyn. und Verwandfer Gebiete*, Aachen, 1929, Berlin (1930).
2. P. Bradshaw, "Effects of streamline curvature on turbulent flow," *AGARDograph*, No. 169 (1973).

3. A. T. Onufriev and S. A. Khristianovich, "On specific features of the turbulent motion in a vortex ring," *Dokl. Akad. Nauk SSSR*, **229**, No. 1, 42–44 (1976).
4. A. T. Onufriev, "On specific features of the motion in the core of a vortex ring," in: *Physical Mechanics, Dynamic Processes in Gases and Solids* [in Russian], No. 4, Izd. Leningrad Univ., Leningrad (1980), pp. 31–69.
5. P. G. Zaets, A. T. Onufriev, M. I. Pilipchuk, et al., "The use of a hot-wire complex coupled with a computer for measurement of the characteristics of turbulent swirling flows," in: *Physical Methods of Studying Transparent Inhomogeneities* [in Russian], Znanie, Moscow (1986).
6. N. A. Safarov, "The behavior of the parameters of a developed turbulent flow in a straight cylindrical channel rotated about its longitudinal axis," Abstract of Candidate's Dissertation in Phys.-Math. Sci., Moscow Phys. Tech. Inst., Moscow (1986).
7. P. G. Zaets, "An experimental study of the turbulence spectrum in a rotating pipe flow," Abstract of Candidate's Dissertation in Phys.-Math. Sci., Moscow Phys. Tech. Inst., Moscow (1986).
8. P. G. Zaets, N. A. Safarov, and R. A. Safarov, "An experimental study of the behavior of the characteristics of turbulent flow in rotating the channel about its longitudinal axis," in: *Modern Problems of Continuum Mechanics* [in Russian], Moscow Phys. Tech. Inst., Moscow (1985), pp. 136–142.
9. W. Rodi, "Turbulence models of the ambient medium," in: *Prediction Methods for Turbulent Flows*, Hemisphere Publishing Corporation (1980).
10. A. F. Kurbatskii, *Simulation of Nonlocal Turbulent Momentum and Heat Transfer* [in Russian], Nauka, Novosibirsk (1988).
11. B. E. Launder, G. J. Reece, and W. Rodi, "Progress in the development of a Reynolds-stress turbulent model," *J. Fluid Mech.*, **68**, 537–566 (1975).
12. M. S. Hossain, "Mathematische modellierung von turbulenten auftriebstromungen," Ph.D. Thesis, University of Karlsruhe, Karlsruhe (1980).
13. M. M. Gibson and B. E. Launder, "Ground effects on pressure fluctuations in the atmospheric boundary layer," *J. Fluid Mech.*, **86**, 491–511 (1978).
14. R. M. C. So and G. J. Yoo, "On the modeling of low-Reynolds-number turbulence," NASA Contractor Report No. 3994 (1986).
15. P. Bradshaw, "The analogy between streamline curvature and buoyancy in turbulent shear flow," *J. Fluid Mech.*, **36**, 177–191 (1969).
16. B. E. Launder, S. H. Priddin, and B. I. Sharma, "The calculation of turbulent boundary layers on spinning and curved surfaces," *Teor. Osn. Inzh. Rasch.* (Transl. *Tr. ASME, Ser. D, J. Basic Eng.*), No. 1, 332–340 (1977).
17. B. J. Daly and F. H. Harlow, "Transport equations in turbulence," *Phys. Fluids*, **13**, No. 11, 2634–2649 (1970).
18. D. B. Spalding, *GENMIX: A General Computer Program for Two-Dimensional Parabolic Phenomena*, Pergamon Press, Oxford (1977).
19. J. Laufer, "The structure of turbulence in fully developed pipe flow," NASA Report No. 1174 (1954).
20. V. I. Bukreev, V. V. Zykov, and V. A. Kostomakha, "One-dimensional laws of velocity fluctuation probability distribution for a turbulent flow in a round pipe," *Izv. Sib. Otd. Akad. Nauk SSSR, Ser. Tekh. Nauk*, **13**, No. 3, 3–9 (1975).
21. M. Schildknecht, J. A. Miller, and G. E. A. Meier, "The influence of suction on the structure of turbulence in fully developed pipe flow," *J. Fluid Mech.*, **90**, 67–107 (1979).
22. C. I. Lawn, "The determination of the rate of dissipation in turbulent pipe flow," *J. Fluid Mech.*, **48**, Part 3, 477–505 (1971).